We are IntechOpen, the world's leading publisher of Open Access books
Built by scientists, for scientists

6,900
Open access books available

185,000
International authors and editors

200M
Downloads

154
Countries delivered to

Our authors are among the

TOP 1%
most cited scientists

12.2%
Contributors from top 500 universities

CLARIVATE ANALYTICS
BOOK CITATION INDEX
INDEXED

WEB OF SCIENCE™

Selection of our books indexed in the Book Citation Index
in Web of Science™ Core Collection (BKCI)

Interested in publishing with us?
Contact book.department@intechopen.com

Numbers displayed above are based on latest data collected.
For more information visit www.intechopen.com

New Prospective Applications of Heterostructures with YBa$_2$Cu$_3$O$_{7-x}$

M. I. Faley, O. M. Faley, U. Poppe, U. Klemradt and
R. E. Dunin-Borkowski

Additional information is available at the end of the chapter

1. Introduction

Among high-T$_c$ superconductors with T$_c$ > 77 K, YBa$_2$Cu$_3$O$_{7-x}$ (YBCO) is the most elaborated material for electric power applications and low noise electronics. Discovered in 1987 [1], YBCO is now included in the most advanced high-T$_c$ superconducting epitaxial oxide thin-film heterostructures with other metal-oxide materials. Cables for electric power transportation, motors, generators and others large scale applications are using 2nd generation flexible superconducting tapes comprising epitaxial YBCO films with critical current about 2 MA/cm^2 at 77 K [2]. Electronic applications of high-T$_c$ superconductors have lower economic impact and received up to now less publicity but they are also becoming competitive. Low noise high-T$_c$ superconducting quantum interference devices (SQUIDs) are made from high quality epitaxial YBCO films and grain boundary Josephson junctions. With a help of a 16-mm multilayer superconducting flux transformer the best magnetic field resolution of high-T$_c$ SQUIDs about 4 fT/√Hz at 77 K was achieved [3]: all-oxide heterostructures based on high-quality epitaxial YBCO thin films with other metal-oxide layers are indispensable for construction of high-T$_c$ SQUIDs with ultimate sensitivity [4]. High-T$_c$ SQUIDs serve as sensors of magnetic field in the LANDTEM geophysical survey system that has located mineral deposits worth Australian \$6bn [5]. Metallic contaminant detection systems are integrated in the food production lines and important for manufacturers of lithium-ion batteries. These systems are gaining sensitivity with high-T$_c$ SQUID sensors [6]. Scanning high-T$_c$ SQUID biosusceptometry is used to track noninvasively labelled colorectal tumors by conducting different preoperative and intraoperative in vivo examinations [7]. In this chapter the prospective applications of epitaxial thin film heterostructures based on YBCO in information technology, electron microscopy and magnetoencephalography are described.
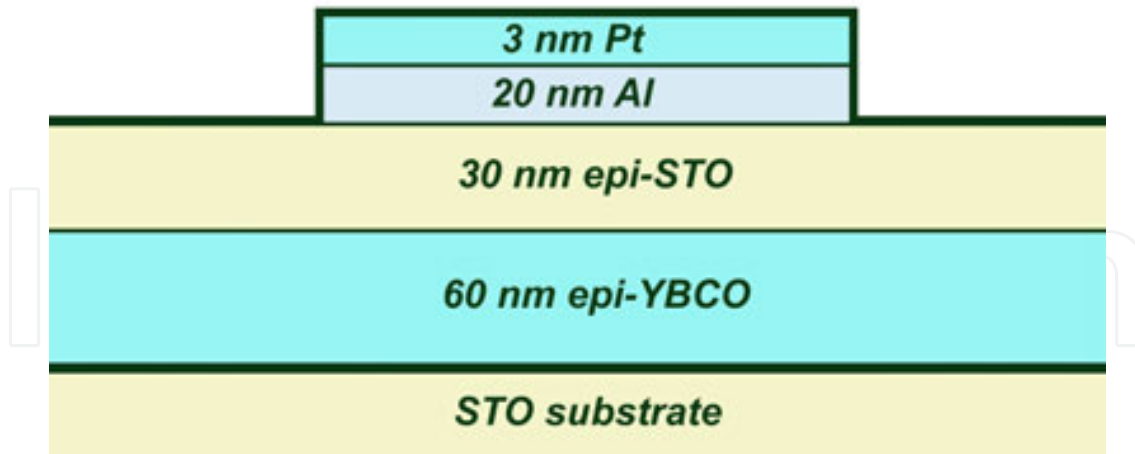
Figure 1. Sketch of YBCO-STO-Al-Pt heterostructure used for the investigation of the resistive switching effect in the present work.

2. Information technology

Storage of information is essential in computers and communication devices which are now indispensable in our everyday life. Resistive switching and the related oxygen motion in $SrTiO_3$ may take place in regions as small as 3 nm [8], [9] which corresponds to a hypothetically possible size of future non-volatile resistive random-access memory (RRAM) memories of about 1 TB/cm². Important attributes of resistive switching elements are the presence of a rectification effect due to a Schottky barrier at one of the interfaces of the insulator with electrodes and the presence of a conducting channel for oxygen vacancies and electrons within the insulator [10], [11]. A large difference between the work functions (WF) of the insulator and the WF of one of the electrodes is required for a pronounced Schottky effect at the interface and a large amplitude of the resistive switching. An advantage of using of YBCO for RRAMs is the high value of its WF ~ 6.1 eV [12], [13]. This value of WF is significantly larger than WFs of Pt or Au electrodes (WF~ 5 eV) and TiO_2 and $SrTiO_3$ (STO) insulators (WF~ 4.3 eV).

Resistive switching memory elements were made using epitaxial thin film heterostructures YBCO-STO-Pt [14]. These elements can operate at room temperature and improve their On/Off resistance switching ratio at lower temperatures. The rectification effect at the interface with YBCO is increasing when YBCO is in the superconducting state [15] giving a hope for further increasing of the On/Off resistance switching ratio. We have produced YBCO-STO-Al-Pt heterostructures (see sketch in Fig.1) and studied their resistive switching and microstructural properties. With YBCO as the bottom electrode a Schottky-like bottom interface is formed whereas the contact between the STO and Al is ohmic: WF of Al is ~ 4.1 eV. A 3 nm thick Pt film served for passivation of Al film.

The YBCO and STO films of the YBCO-STO-Al-Pt heterostructure were prepared by high oxygen pressure DC magnetron sputtering technique [16], [17]. The YBCO electrode was grounded using ohmic contact with a silver pad and a piece of indium. 20-μm-square top

electrodes consisting from Al and Pt films were deposited on STO by DC magnetron sputtering in pure argon and patterned by deep-UV photolithography and ion beam etching. The patterning was finished by removing of the residuals by chemical etching of aluminium film with developer for AZ photoresist AZ326MIF. Electrical contact to the top electrode was performed by a flexible Pt wire using a micromanipulator and an optical microscope. The electrical measurements were performed at room temperature in ambient atmosphere.

Pristine contacts have a resistance of about 100 GOhm. Activation of the memory cells was performed by the process of electrodegradation (electroforming) of the STO insulator at a negative voltage of −6 V and a compliance current of 6 mA. Opposite polarity did not activate the cells but irreversibly destroyed them by formation of oxygen bubbles at the STO-Al interface. Only one conducting channel appeared at each contact pad as the result of electro-forming and the position of this channel was beyond traces of Pt wire in the top electrode. The I(V) and R(V) characteristics of the YBCO-STO-Al-Pt heterostructure are shown in Fig. 2 and Fig. 3 respectively. All contacts have demonstrated similar characteristics.
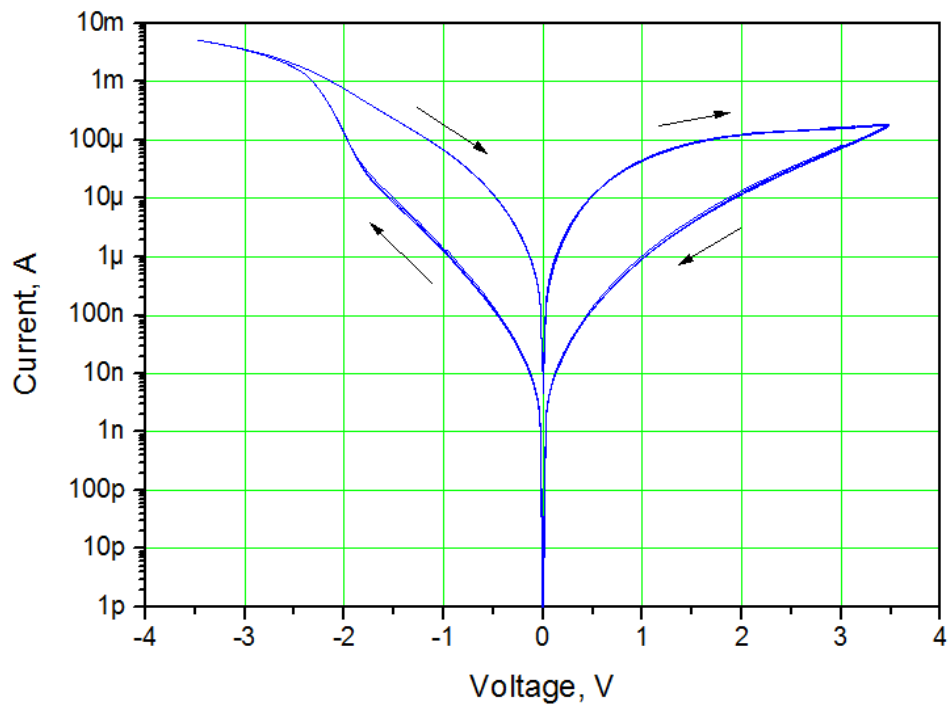

Figure 2. I(V)-characteristics of YBCO-STO-Al-Pt heterostructure demonstrating five continuous resistive switching cycles.

Scanning electron microscopy of the electroformed area was performed in the lower secondary electron image (LEI) mode (see Fig. 4). A conducting channel with diameter ~400 nm through STO film and a trace of overheated area near this channel were observed. Investigation of the conducting channel and its interfaces with electrodes by cross-sectional high resolution transmission electron microscopy will give more information about the microstructure and physical nature of operation of the resistive switching effect in these contacts.
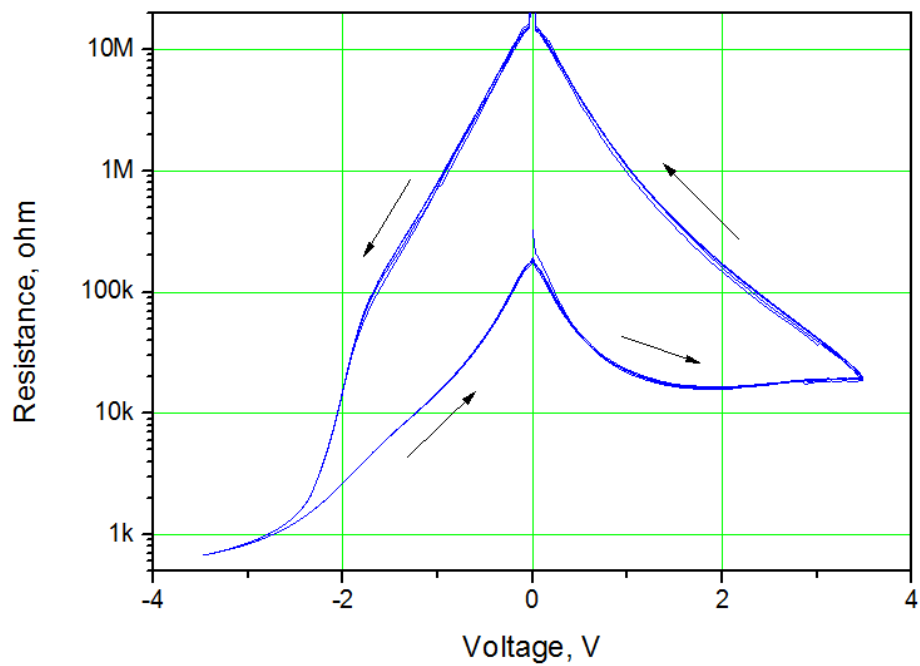
Figure 3. R(V)-characteristics of YBCO-STO-Al-Pt heterostructure demonstrating five continuous resistive switching cycles.
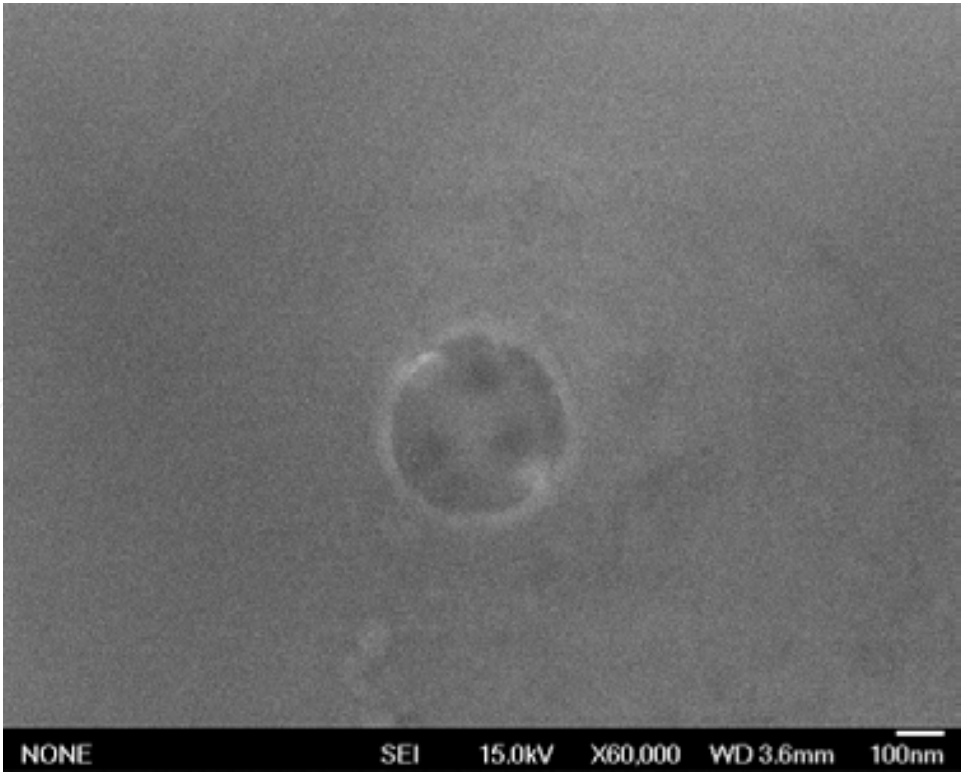

Figure 4. SEM image of the electroformed area of YBCO-STO-Al-Pt heterostructure performed in the LEI mode.

A possible mechanism of the observed resistive switching effect in the YBCO-STO-Al-Pt heterostructure can be the following. During the process of electrodegradation, a conducting channel through the STO film separated by a highly ohmic Schottky barrier from the bottom electrode is formed. The nature of the conducting channel is described elsewhere [11]. The conducting channel serves for a transport of electrons and oxygen ions by the switching electric fields. The reactions of creation (at negative bias) and dissociation (at positive bias) of oxygen vacancies near the bottom interface probably lead to the greatest contribution to the On/Off resistance switching ratio of the described contacts. A part of oxygen atoms can migrate through the bottom interface while the other part can be accommodated inside STO leading to local strain and elastic deformation of STO lattice near the bottom interface. Serving as a reservoir of oxygen atoms, the high value of the work function and the mechanical strength of YBCO are favourable for the superior operation, reproducibility and long term stability of the resistive switching elements described above.

3. Electron microscopy

Modern fifth-order aberration-corrected high resolution transmission electron microscopy (TEM) is able to resolve a crystal spacing less than 50 pm [18]. Especially correction of chromatic aberrations is considered as extremely challenging technological task. The complicated electron optics, extreme machining precision and stability for the power supplies are in the sub 0.1 ppm range are required. One possibility for the further improvement of the resolution of TEM will depend on ability to suppress fluctuations of magnetic fields along the optic axis and especially in magnetic lenses [19]. Some of the magnetic fluctuations are related to thermal fluctuations (Johnson-Nyquist noise) and can be reduced by cooling of the microscope column and lenses to cryogenic temperatures [19].

The temporal stability of magnetic fields in magnetic lenses is limited by several sources of interference, including fluctuations of the current in their coils and the fact that a ferromagnetic yoke can act as an antenna, which couples external electromagnetic interference or magnetic fields generated by movable magnetic objects to the electron beam. Both the movement of magnetic domains (Barkhausen noise) and thermal current fluctuations (Johnson-Nyquist noise) inside the yoke can lead to statistical fluctuations of the magnetic flux that propagates through it. In addition, since the permeability of the yoke is temperature-dependent, fluctuations in temperature can result in variations in the magnetic field in the lens.

We investigate a new approach for improving the performance of magnetic lenses for electron microscopy and other applications where highly stable magnetic fields are required. We have proposed using superconducting rings around the ends of the pole piece to stabilize magnetic fields in the ferromagnetic yokes of magnetic lenses for electron microscopy [20]. Our proposal involves introducing a superconducting ring around a ferromagnetic yoke, in which the magnetic flux should remain constant to a much greater precision than the stability of conventional power supplies allows. Fluctuations of the magnetic field in the yoke induce a current in the superconducting ring, which results in an oppositely directed magnetic flux in

the yoke that exactly compensates these fluctuations. Because the superconductor has no resistance, the induced current can flow indefinitely and the magnetic field in the ferromagnetic yoke can be maintained indefinitely. In this way, the current induced in the superconducting ring compensates fluctuations in the magnetic field, while the required DC value of the magnetic field is provided by the coils. By positioning the superconducting ring outside the magnetic field of the lens, dissipation of the induced currents due to creep of Abrikosov vortices can be avoided.

This new concept originates from the phase coherence of Cooper pairs in superconductors and dependence of Berry's phase of charged particles on magnetic vector potential. As a consequence, magnetic flux through closed ring of superconductor is automatically kept constant due to exact compensation of changes in external magnetic field by persistent superconducting current induced in the superconducting ring (see Fig. 5) [21].
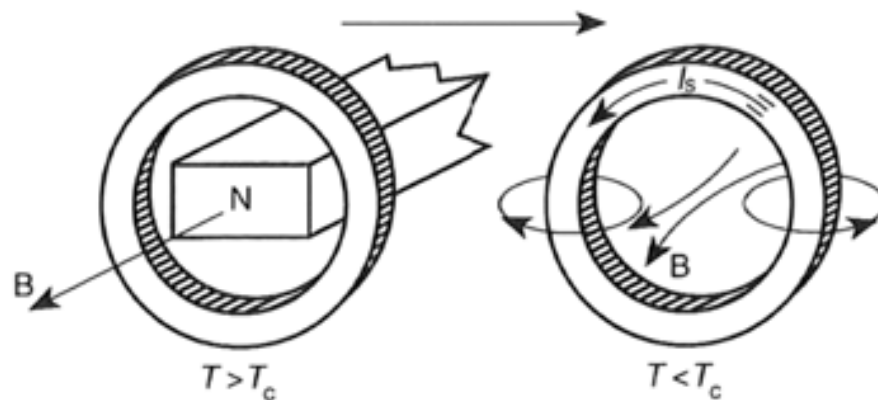

Figure 5. Excitation of persistent current in a superconducting ring [21].

This ability of a superconductor to keep magnetic flux constant can be visualised by a demonstrative experiment shown in Fig. 6. The magnetic field induced by the persistent current in YBCO forces the substrate to maintain its position relative to the magnet constant in spite of the counteracting influence of gravitation.

A simple computer simulation of magnetic field of source of fluctuating magnetic fields (1) and ferromagnetic core (2) depending on the presence of superconducting stabilizer (3) was performed (see Fig. 7). This simulation qualitatively shows that superconducting rings practically eliminate fluctuating magnetic fields in the gap (4). Due to high permeability of ferromagnet (~10000) the major part of the magnetic flux through superconducting ring is concentrated inside the ferromagnetic yoke. Induced superconducting currents keep magnetic flux penetrating through the rings constant and this eliminates fluctuations in the gap (4).

A "proof-of-principle" demonstration of the proposed approach was achieved by using the experimental setup shown in the form of a schematic diagram and a photograph in Figures 8a and 8b, respectively. A high-T_c DC SQUID [3] operating at a temperature of 77 K was placed in the vicinity of a gap in a nanocrystalline VITROPERM core VAC W867-01 and used for sensitive non-invasive characterisation of the magnetic field in the stabilized region. Two
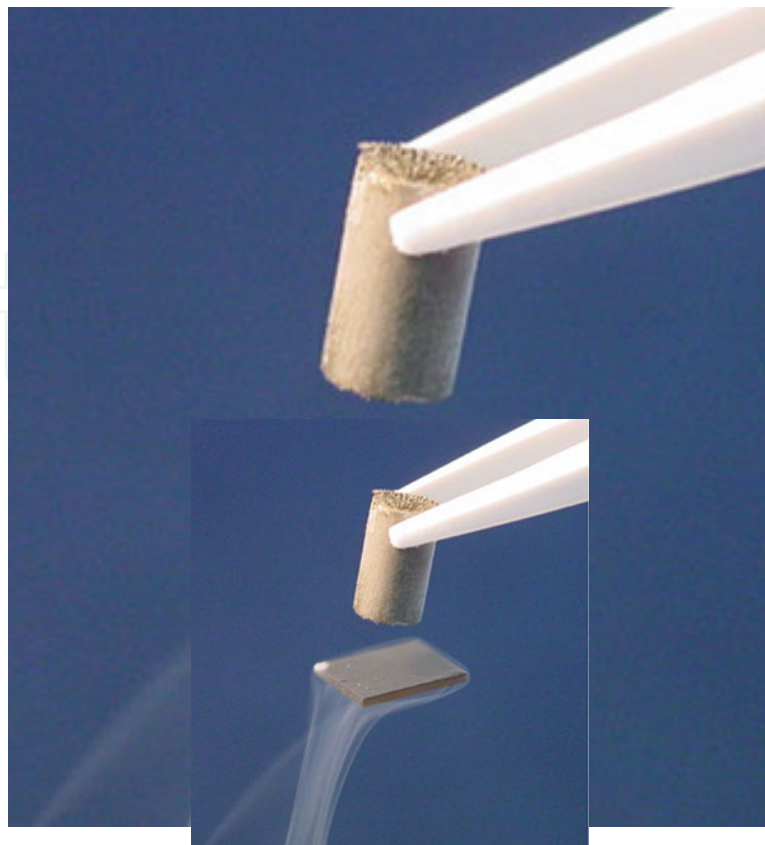
Figure 6. Levitation of 1 cm^2 substrate with 100 nm YBCO film under SmCo$_5$ permanent magnet.
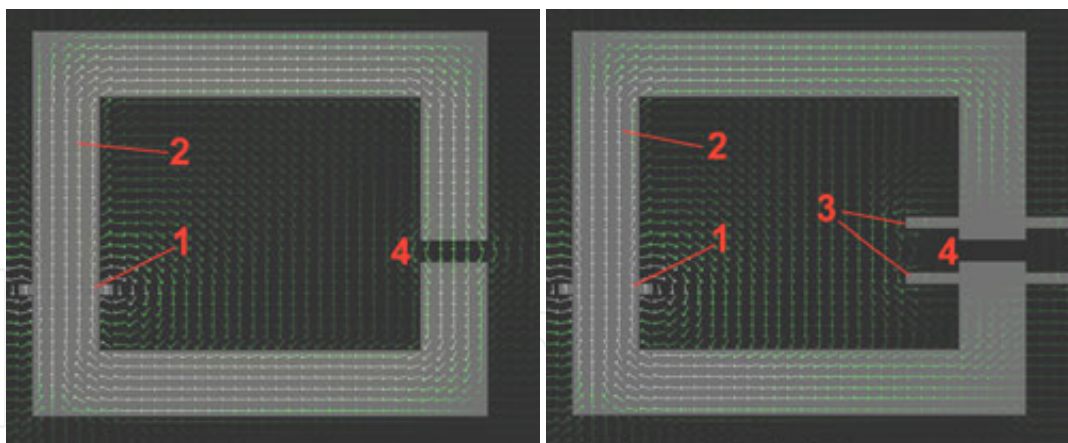

Figure 7. Computer simulation of magnetic fields of source of fluctuating magnetic fields (1) with a ferromagnetic core (2) without superconducting stabilizer (left picture) and with superconducting stabilizer (3) (right picture).

A simple computer simulation of magnetic field of source of fluctuating magnetic fields (1) and ferromagnetic core (2) depending on the presence of superconducting stabilizer (3) was performed (see Fig. 7). This simulation qualitatively shows that superconducting rings practically eliminate fluctuating magnetic fields in the gap (4). Due to high permeability of ferromagnet (~10000) the major part of the magnetic flux through superconducting ring is concentrated inside the ferromagnetic yoke. Induced superconducting currents keep magnetic flux penetrating through the rings constant, and this eliminates fluctuations in the gap (4).

A "proof-of-principle" demonstration of the proposed approach was achieved by using the experimental setup shown in the form of a schematic diagram and a photograph in Figures 8a and 8b, respectively. A high-T$_c$ DC SQUID [3] operating at a temperature of 77 K was placed in the vicinity of a gap in a nanocrystalline VITROPERM core VAC W867-01 and used for sensitive non-invasive characterisation of the magnetic field in the stabilized region. Two serially connected platinum thermometers PT-100 were used as local heating elements. The heating element was glued on superconducting ring and thermally insulated from liquid nitrogen by silicone glue.

a temperature of 77 K was placed in the vicinity of a gap in a nanocrystalline VITROPERM core VAC W867-01 a[...]ed for sensitive non-invasive characterisation of the magnetic field in the stabilized region. Two serially connect[...]tinum thermometers PT-100 were used as local heating elements. The heating element was glued on superconducti[...]g and thermally insulated from liquid nitrogen by silicone glue.

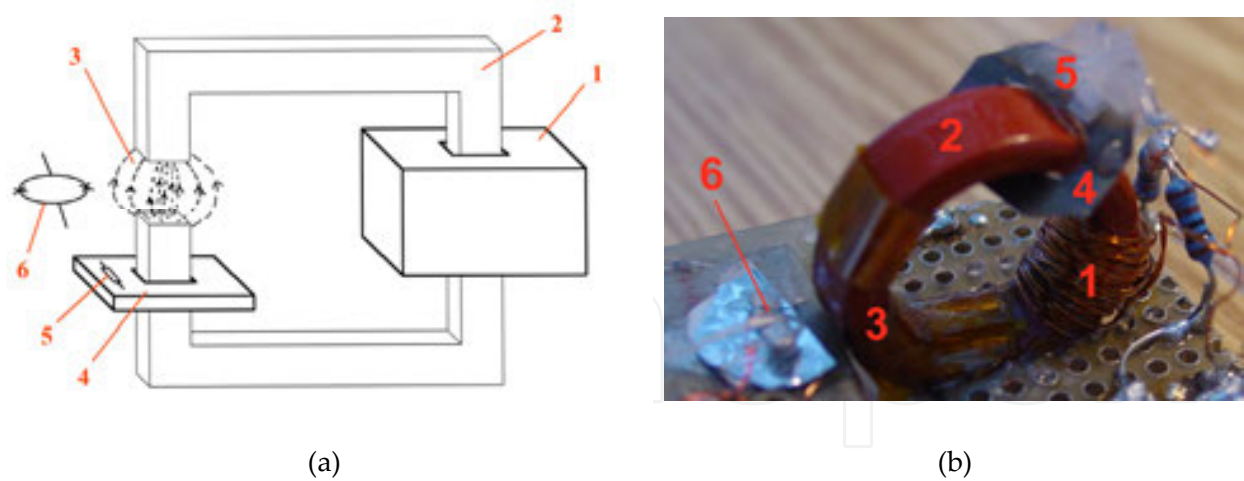(a)   (b)

Figure 8. (a) Sketch of experimental setup with main field coil (1), soft magnetic yoke (2), stabilized magnetic field region (3), superconducting ring (4), local heating element to allow flux entrance into the superconducting ring for a change of detector (6) to monitor the flux in the stabilized region. (b) Photograph of experimental setup, which was placed in liquid nitrogen for the measurement.
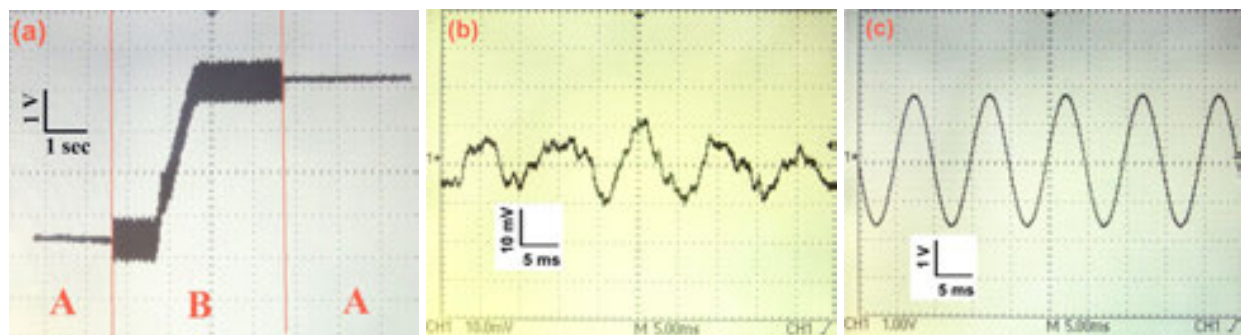

Figure 9. (a) Oscillogram showing measured magnetic field in stabilized (A) and adjusted (B) modes in the test setup. B, the additional interference, which was simulated by adding an AC field to the main (DC) field of the coil, appears. The field was then also changed to a different value during heating of the superconducting ring. (b) Test signals with SC stabilizer ON and (c) with SC stabilizer OFF.

Figure 9 demonstrates the operation of the superconducting magnetic field stabilizer. Magnetic field fluctuation was simulated by adding an alternating current (AC) field (~100 Hz) to the main DC field of the coil. The ring was made from a YBa$_2$Cu$_3$O$_7$ high-T$_c$ thin film tape that was cooled to 77 K in stabilizing mode A. Optimized demonstrator shown in figure 8 by more than 90 % of the magnetic field fluctuations were suppressed in stabilizer when compared to mode B, in which the superconducting ring was switched to its normal state above the superconducting transition temperature. In mode B, adjustment to a new magnetic field value was shown in figure 9a. Figure 9b shows the magnetic field in mode A and figure 9c shows the magnetic field in mode B measured with 5 ms time scale.

Schematic representation of commercially available 2nd generation flexible YBa$_2$Cu$_3$O$_7$ high-T$_c$ thin film tape which was used for preparation of superconducting (SC) rings in the present study is shown in figure 10 [22]. The 100 mm wide and 100 μm thick stainless steel Hastelloy substrate is covered by a solution deposition planarization (SDP) layer to reduce surface roughness on to nanometer level. Buffer layer of 200 nm MgO film is prepared by ion beam (IBAD) method followed by epitaxial growth. Epitaxial 3 μm thick YBCO film is deposited on M[...] evaporation process and covered by 1μm silver film. The tape is able to transport persistent super[...] over 500 A/cm at 77 K. We have patterned superconducting rings from such tape by laser cutter m[...] diamond file.

roughness on to nanometer level. Buffer layer of 200 nm MgO film is prepared by ion beam assisted deposition (IBAD) method followed by epitaxial growth. Epitaxial 3 μm thick YBCO film is deposited on MgO by reactive co-evaporation process and covered by 1μm silver film. The tape is able to transport persistent superconducting current over 500 A/cm at 77 K. We have patterned superconducting rings from such tape by laser cutter machine and/or by a diamond file.
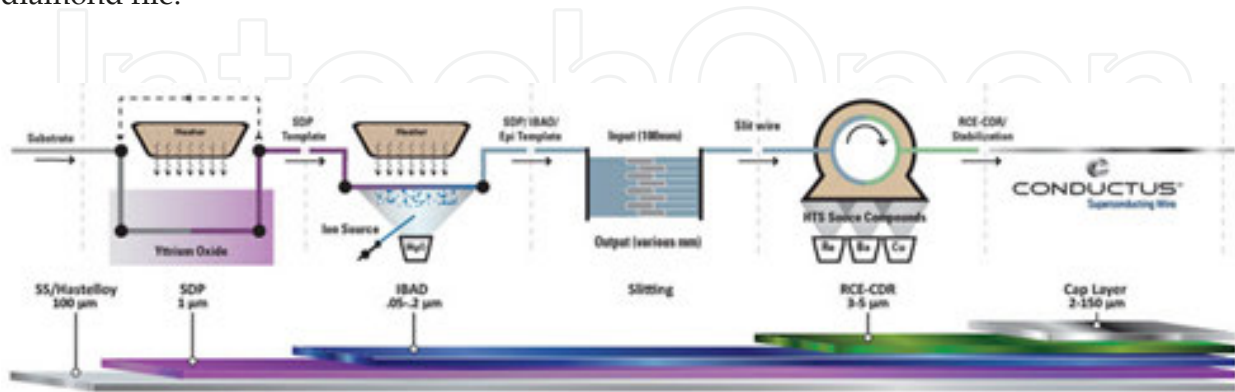

Figure 10. Schematic representation of the Conductus® superconducting wire manufacturing process for commercially available YBa$_2$Cu$_3$O$_7$ high-T$_c$ thin film tapes [22].

Advantage of application of superconducting tapes for magnetic field stabilizer is their low costs (~100$/m), flexibility, high critical current and possibility of patterning by a simple mechanical machining. Currently, up to 12 mm wide tapes are commercially available. Up to 10 cm wide tapes with complete heterostructure including YBCO are expected to appear soon on market. Single crystal wafers with epitaxial YBCO films can be also used but they are much more expensive, thicker and brittle.

The superconducting magnetic field stabilizer can be applied to several types of scanning electron microscope or transmission electron microscope (TEM) lenses. Sketches of prospective setups for objective lens are shown in figures 11 – 15 [20].
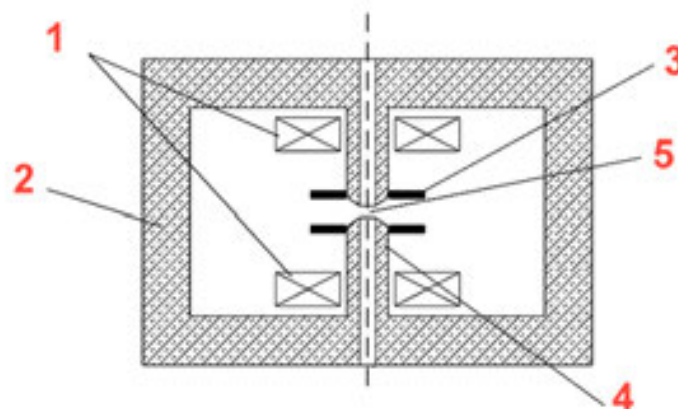

Figure 11. Sketch of prospective setup for a TEM objective lens [20]. Coils (1) provide magnetic flux through the yoke (2). Two stabilizing SC rings (3) are placed near the pole piece ends (4) to stabilize magnetic field in the sample area (5).
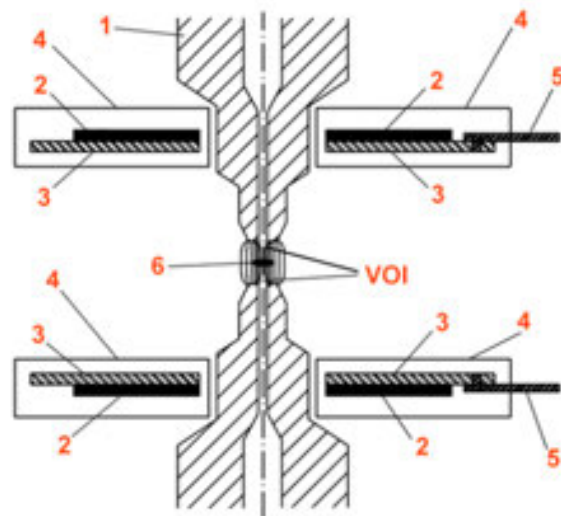
Figure 12. Sketch of prospective setup for a TEM objective lens [20]. The coils (not shown) providing the main magnetic flux through the yoke (1). The poles are surrounded by SC rings (2), which are placed on heat conducting substrates (3) inside thermal insulations (4) and cooled through cold leads (5). Magnetic field is stabilized in volume of interest (VOI) near the sample (6).
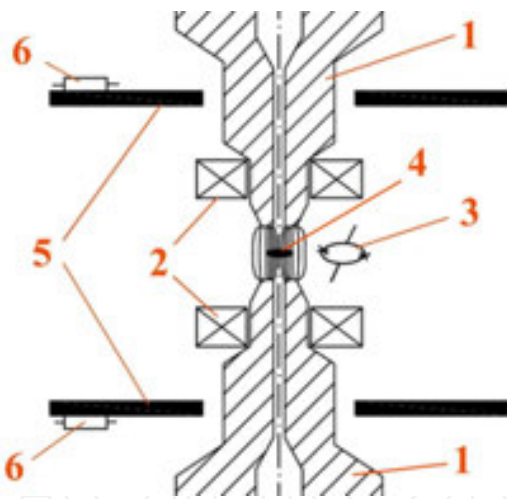

Figure 13. Sketch of prospective setup for a TEM objective lens [20]. Apart from the coils (not shown) providing the main magnetic flux through the yoke (1), two additional coils (2) can be used together with a SQUID detector (3) in feedback mode for fine adjustment of the magnetic lens field near the sample (4). Two stabilizing SC rings (5) with local resistive heaters (6) are placed near the pole piece ends.

There is still a long way to actual implementation of superconductivity for electron microscopy. The superconducting magnetic field stabilizer and cooling elements should fit into modern complicated array of electron lenses and realized with the same extreme machining precision as other parts of the electron microscopes. But the requirement of further improving of resolution of electron microscopes may prevail and, sooner or later, make this way beneficial.
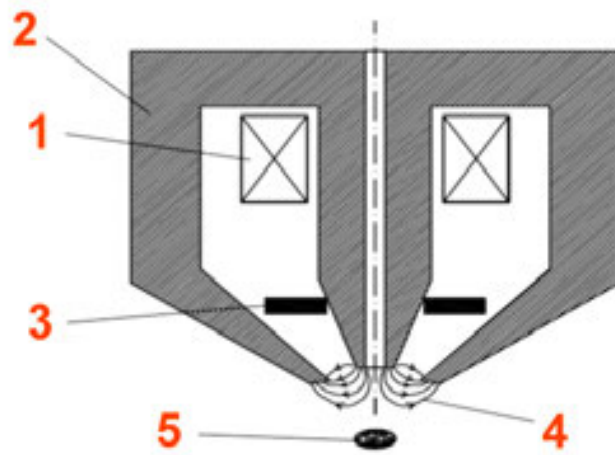
Figure 14. Sketch of prospective setup for an SEM conical objective lens [20]. Coil (1) provides magnetic flux through a yoke (2). A stabilizing SC ring (3) is placed near the pole piece end to stabilize the magnetic field in the area of the strong magnetic field gradient (4), which focuses the electron beam onto the sample.
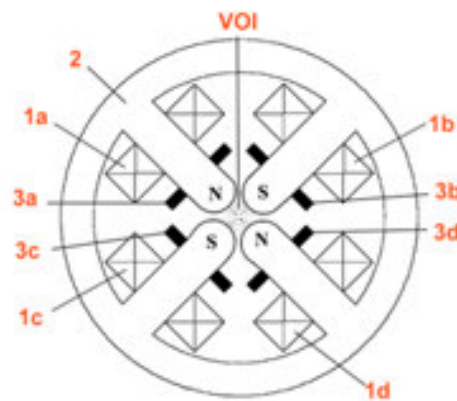

Figure 15. Sketch of prospective setup for a quadrupole lens [20]. Coils (1a-d) provide magnetic flux through the yoke (2). Stabilizing SC rings (3a-d) are placed near the pole piece ends (S, N) to stabilize the magnetic fields and their gradients in the volume of interest (VOI).

4. Magnetoencephalography (MEG)

The importance of developing a new generation of non-invasive imaging techniques that can be used to understand human brain function is reflected, for example, in the "Human Brain Project" (EU) and the "BRAIN Initiative" (USA). Multichannel MEG systems that are based on low temperature SQUIDs are well developed and routinely used for the non-invasive investigation of multiple time-dependent sources of weak magnetic field generated by the human brain. MEG systems that are based on sensitive high-T$_c$ SQUIDs promise to improve signal-to-noise ratio and to provide better source characterization by reducing the SQUID-to-scalp separation [23]. In a high-T$_c$ system, one can achieve significant savings in energy and operational cost, in particular by avoiding problems with the supply of liquid helium [24, 25]. A single-channel MEG system based on high-T$_c$ DC SQUID flip-chip magnetometers with a

16 mm x 16 mm multilayer flux transformer has achieved a magnetic field resolution of ~ 4 fT/√Hz at 77.4 K [26, 3], which is similar to the magnetic field resolution of individual channels in commercial MEG systems based on 28 mm x 28 mm low-T_c SQUIDs [27].

The magnetic signals that are detected by MEG originate from neocortical columns, each of which consists of ~50,000 pyramidal cells with a net current ~10 nA. The magnetic fields measured by MEG are ~ 100 fT in the frequency range 1 Hz to 1 kHz. A spatial resolution of the MEG system of a few mm for such sources is usually sufficient. These values result in mutually dependent restrictions on the sensitivity, size and positioning of the SQUIDs: a reduction in the size of the sensors and in their proximity to the neural sources in the brain can partially compensate for a loss in sensitivity. On the other hand, more sensitive sensors allow for greater flexibility in the construction of the system. High-T_c SQUIDs can be cooled in cryostats that have fewer radiation shields and can be placed much closer to the outer wall than low-T_c SQUIDs. Assuming a similar field resolution and similar sizes of the sensors, the signal-to-noise ratio obtained during the detection of superficial and/or shallower sources of neuromagnetic signals by a high-T_c MEG system can be higher than for a low-T_c MEG system. At least 40% more information can be obtained using a high-T_c MEG system when compared to the state-of-the-art in low-T_c MEG systems [28].

The first source localization of brain activity using a single channel high-T_c system for MEG was demonstrated recently [29]. Taking into consideration possible systematic temporal drifts in the physiological and functional condition of the investigated brain area during the measurements, at least ten simultaneously operating channels are required for better diagnosis in practical applications of high-T_c MEG systems: for example, 7 signal channels and 3 reference channels. The construction of high-T_c MEG systems with more than 100 channels would be the next step in this development. However, multichannel high-T_c MEG systems have not yet been realized because of a number of issues associated with the integration of high-T_c SQUID magnetometers into the dense arrays of sensors that are required for MEG systems. Here, we describe these problems and suggest some solutions. First, we describe the properties of high-T_c SQUIDs that are essential for the construction of multichannel systems. Several issues, including crosstalk between the sensors, vibration-free cooling of sensors, minimization of the sensor-to-object distance, as well as optimization of the sensor positions and gantry design, are discussed.

In a sufficiently magnetically well shielded room, it is preferably to use magnetometers instead of gradiometers for improved sensitivity to deep and/or distant sources. The magnetometers can be made fully with thin film technology, avoiding the use of superconducting wires. This results in comparable capabilities for high-T_c and low-T_c SQUIDs.

Multichannel high-T_c MEG systems comprise many high-T_c SQUIDs, some of which may require replacement over time. Although the technology required for producing low noise high-T_c SQUID magnetometers for MEG has been developed (see [3] and [30] and references therein), it is still not a mass production technology. Scaling to a higher production rate can be achieved by using parallel processing and/or larger single crystal MgO wafers, which are available in sizes of up to ~10 cm. High oxygen pressure sputtering allows deposition of large homogeneous areas of high-quality stoichiometric epitaxial heterostructures of superconduct-

ing cuprates with a mirror-like surface and superior electron transport properties [16]. The typical superconducting transition temperatures and critical current densities of YBa$_2$Cu$_3$O$_{7-x}$ (YBCO) films obtained by this method are ~93 K and ~6 10^6 A/cm^2 at 77.4 K, respectively.

The most suitable high-T$_c$ SQUID magnetometers for multichannel systems from a price and quality point of view were recently developed [3]. These SQUIDs are based on high-T$_c$ step-edge Josephson junctions, which are fabricated from specially oriented YBCO films grown on graphoepitaxially buffered steps on MgO substrates [30], [31]. The predecessors of such junctions were developed in the CSIRO group (see [32] and references therein). The cross-sectional areas of the graphoepitaxial junctions used in the SQUIDs are ~ 0.1 μm^2, which is about two orders of magnitude smaller than the cross-sectional area of typical Nb-based low-T$_c$ junctions. Step edge junctions are also characterized by a larger normal state resistance R$_n$ ~20 Ohm, a higher I$_c$R$_n$ of ~ 0.6 mV at 77.4 K and a lower capacitance C of ~10 fF, when compared to bicrystal high-T$_c$ Josephson junctions [30]. The high resistance of these junctions leads to large voltage swings of the SQUIDs (by ~ 50 μV), but it promotes coupling to radio-frequency (RF) electromagnetic interference and results in the need for measures to achieve better RF filtering and shielding. The low capacitance of the Josephson junctions is advantageous for lowering the intrinsic flux noise of DC SQUIDs [33], [34]:

$$S_\Phi \approx 32 k_B T L (LC / \beta_C)^{1/2}, \qquad (1)$$

where $\beta_C = 2\pi I_C R_n^2 / \Phi_0 \approx 0.4$ is the McCumber parameter and Φ_0=2.07 10^{-15} T m^2 is the magnetic flux quantum. The lower operating temperatures of low-T$_c$ SQUIDs are almost compensated by the typically much higher capacitance of their Josephson junctions (~ 1 pF). This property can explain the comparably high sensitivities of high-T$_c$ and low-T$_c$ SQUIDs in spite of the much higher operating temperature of high-T$_c$ SQUIDs.
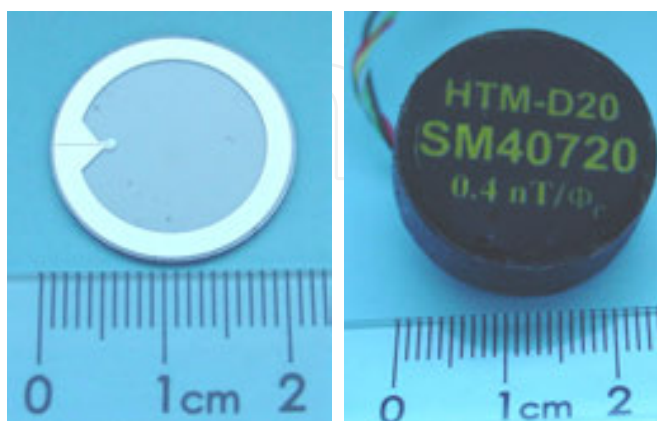

Figure 16. A multilayer high-Tc superconducting flux transformer with a 20 mm pick-up loop and a 14-turn input coil (left photograph) and an encapsulated DC SQUID magnetometer containing such a flux transformer (right photograph).

In MEG systems, near-optimal sensitivity of SQUIDs to magnetic fields can be provided by a superconducting flux transformer with a 14-turn input coil and a pick-up loop with an outer diameter of 20 mm. Figure 16 shows a photograph of such a flux transformer and a vacuum-tight encapsulated high-T$_c$ magnetometer (type HTM-D20) intended for assembly into a multichannel MEG system. The capsule has an outer diameter of ~24 mm, which is smaller than the 27-mm capsule for 16-mm magnetometers of type HTM-16 [35]. It encloses a flip-chip magnetometer, a feedback coil and a heater. The magnetometer consists of a 20 mm flux transformer that is inductively coupled to the high-T$_c$ SQUID, as described in [3].

In MEG systems, near-optimal sensitivity of SQUIDs to magnetic fields can be provided by a superconducting flux transformer with a 14-turn input coil and a pick-up loop with an outer diameter of 20 mm. Figure 16 shows a photograph of such a flux transformer and a vacuum-tight encapsulated high-T_c magnetometer (type HTM-D20) intended for assembly into a multichannel MEG system. The capsule has an outer diameter of ~24 mm, which is smaller than the 27-mm capsule for 16-mm magnetometers of type HTM-16 [35]. It encloses a flip-chip magnetometer, a feedback coil and a heater. The magnetometer consists of a 20 mm flux transformer that is inductively coupled to the high-T_c SQUID, as described in [3].
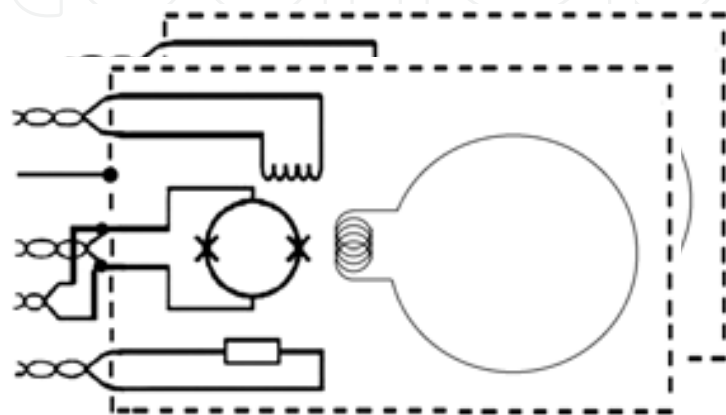

Figure 17. Schematic diagram of a vacuum-tight encapsulated SQUID with a superconducting flux transformer, a feedback coil, a heater and a grounded RF shield.
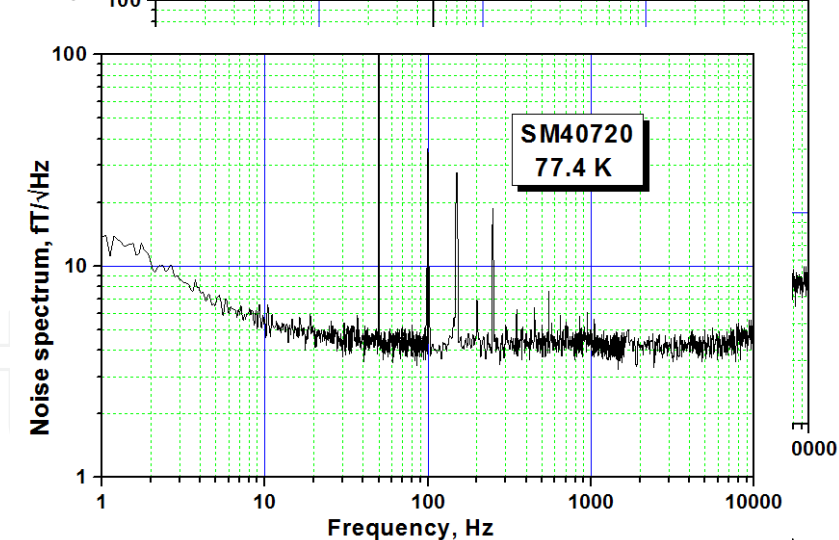
Figure 18. Noise spectrum of an encapsulated HTM-D20 magnetometer in a superconducting shield.

A schematic diagram of an encapsulated SQUID flip-chip magnetometer is shown in Figure 17. The 10-turn modulation and feedback coil has a diameter of 3 mm and is coupled directly to the SQUID. The magnetometer has a sensitivity of ~0.4 nT/Φ and a magnetic field resolution of ~4 fT/√Hz at 77.4 K (see 18). The measurement of the noise spectrum was performed inside a 3-layer μ-metal shield and an YBCO superconducting shield.

In multi-channel SQUID systems, an important requirement is to prevent crosstalk between channels. Decoupling of the output signal of each SQUID in a multichannel system is provided by modulation and feedback. Decoupling of a SQUID from its feedback coils. Parasitic inductive coupling between the feedback coil and the input neighboring sensors should be minimized. Such coupling can be expressed in terms of crosstalk between sensors in terms of the ratio between the flux induced by the feedback coil in a test sensor Φ_1 by a nearby inducing and the flux read by the inducing sensor Φ_2:

$$\frac{\Phi_1}{\Phi_2} = \frac{M_{1,2}}{M_{1,1}} \approx \frac{\Phi_1^{pu}}{\Phi_2^{pu}}, \quad (2)$$

Dummy Text where Φ_1^{pu} and Φ_2^{pu} are the fluxes in the pick-up loops of these two sensors, $M_{1,1}$ is the

In multi-channel SQUID systems, an important requirement is to prevent crosstalk between channels. Linearization of the output signal of each SQUID in a multichannel system is provided by modulation and feedback signals to each SQUID from its feedback coils. Parasitic inductive coupling between the feedback coil and the pick-up of the neighboring sensors should be minimized. Such coupling can be expressed in terms of crosstalk between the SQUID sensors in terms of the ratio between the flux induced by the feedback coil in a test sensor Φ_1 by a nearby inducing sensor and the flux read by the inducing sensor Φ_2:

$$\frac{\Phi_1}{\Phi_2} = \frac{M_{1,2}}{M_{1,1}} \approx \frac{\Phi_1^{pu}}{\Phi_2^{pu}}, \tag{2}$$

where Φ_1^{pu} and Φ_2^{pu} are the fluxes in the pick-up loops of these two sensors, $M_{1,1}$ is the mutual inductance between the feedback coil and the sensing coil of the inducing SQUID and $M_{1,2}$ is the mutual inductance between the feedback coil of the inducing SQUID and the sensing coil of the test sensor (see Figure 19).

Low crosstalk operation of SQUID arrays requires low values of $M_{1,2}$ and at the same time high values of $M_{1,1}$. The highest value of $M_{1,1}$ is generally provided by coupling the relatively large feedback coil to a pick-up loop that has a similar size, but in this case the value of $M_{1,2}$ is unacceptably high. With a fixed size of feedback coil, any increase in $M_{1,1}$ results in an increase in $M_{1,2}$. In this work, we propose a 3-mm multi-turn feedback coil that is inductively coupled to a 3-mm direct coupled pick-up loop of the SQUID [3].
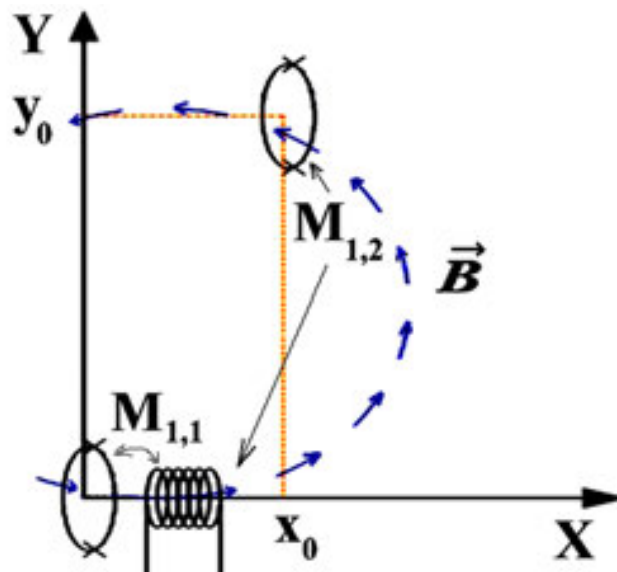

Figure 19. Schematic diagram of the setup for measuring crosstalk.

The feedback coil can be described as a magnetic dipole with a magnetic moment. $|\vec{m}|=IN\pi r^2$ and a magnetic field

$$\vec{B} = \frac{\mu_0}{4\pi} \left[\frac{3(\vec{m}\vec{L})\vec{L}}{L^5} - \frac{\vec{m}}{L^3} \right], \tag{3}$$

where $\vec{L}$ is the distance from the dipole to the point of measurement, $\mu_0 = 4\pi\ 10^{-7}$ H/m, N=10 is the number of turns in modulation coil, and r=1.5 mm is the radius of the feedback coil and the pick-up loop of the SQUID. The crosstalk is:

$$\frac{\Phi_1^{pu}}{\Phi_2^{pu}} \approx \frac{\mu_0 m}{4\pi\Phi_2^{pu}} \int\limits_{y_0-R}^{y_0+R} \int\limits_{-\sqrt{R^2-(y-y_0)^2}}^{\sqrt{R^2-(y-y_0)^2}} \frac{2x_0^2 - y^2 - z^2}{\left(x_0^2 + y^2 + z^2\right)^{5/2}} dzdy, \tag{4}$$

where R=1 cm is the radius of the pick-up loop of the neighboring magnetometer. The flux Φ_2 induced by the feedback coil in the pick-up loop of the inducing SQUID is:

$$\Phi_2^{pu} \approx \frac{\mu_0 m r^2}{2\left(r^2 + x_0^2\right)^{3/2}}. \tag{5}$$

The result of the calculation of Eqs. (4) and (5) is shown in Figure 20, while experimentally measured data for Φ_1 / Φ_2 are shown in Figure 21.

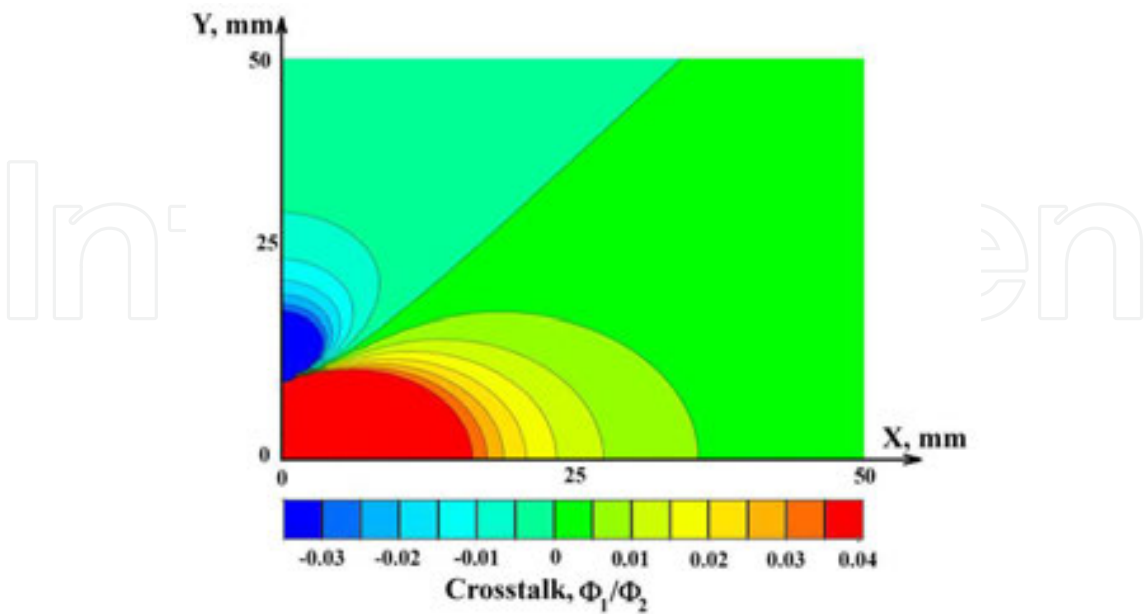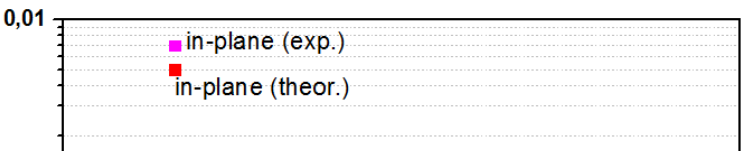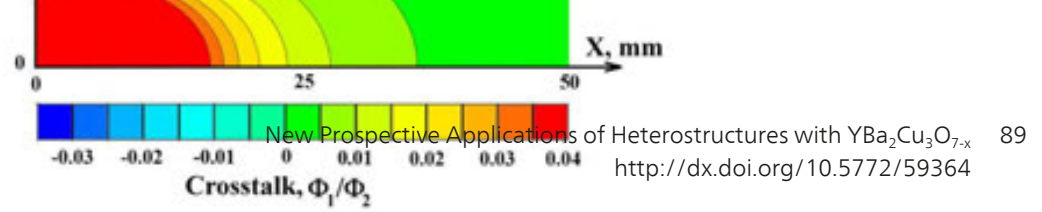Figure 20. Crosstalk calculation according to Eqs. (4) and (5).
Figure 20. Crosstalk calculation according to Eqs. (4) and (5).

A crosstalk of below 1 % was achieved at distances of more than 30 mm in both orientations. This meas the possibility to build close-packed arrays of high-T$_c$ SQUID magnetometers with the proposed feedback coil.

A crosstalk of below 1 % was achieved at distances of more than 30 mm in both orientations. This measurement confirms the possibility to build close-packed arrays of high-T$_c$ SQUID magnetometers with the proposed configuration of feedback coil.
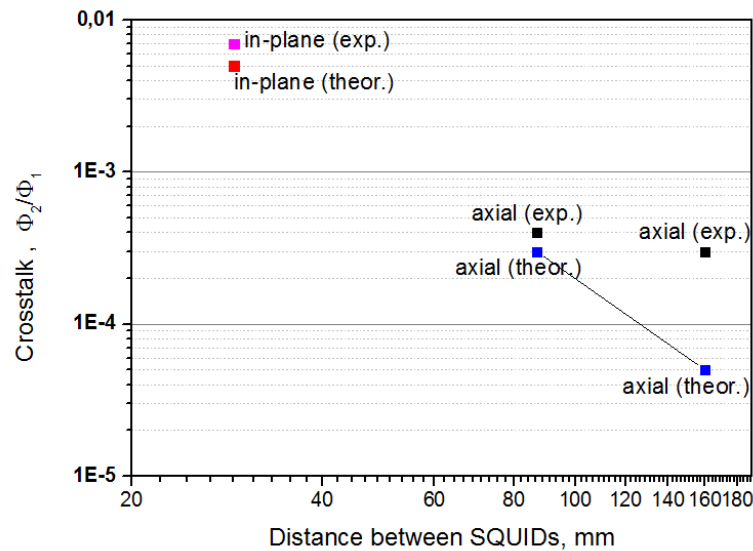

Figure 21. Experimentally measured crosstalk for different positions of neighbouring sensors and corresponding estimations: 1.) (■, ■) for a coplanar orientation (along the Y-axis in Figure 19) and 2.) (■, ■) for an axial orientation (along the X-axis).

In order to take full advantage of high-T$_c$ SQUIDs, they should be placed in a dense array as close as possible to the scalp and to neighboring sensors. More than 100 encapsulated HTM-D20 magnetometers can be arranged around the head of an adult human (see Figure 22). The problem is the variety of individual sizes of heads that should be accommodated in a mechanically adjustable MEG system to maintain close proximity of the sensors to the scalp.

Figure 22. Example of positioning more than 100 encapsulated HTM-D20 magnetometers around a 3D model of the head of an adult human.

•Figure 23. Schematic view of an array of HTM-D20 magnetometers cooled sidewards in the vacu

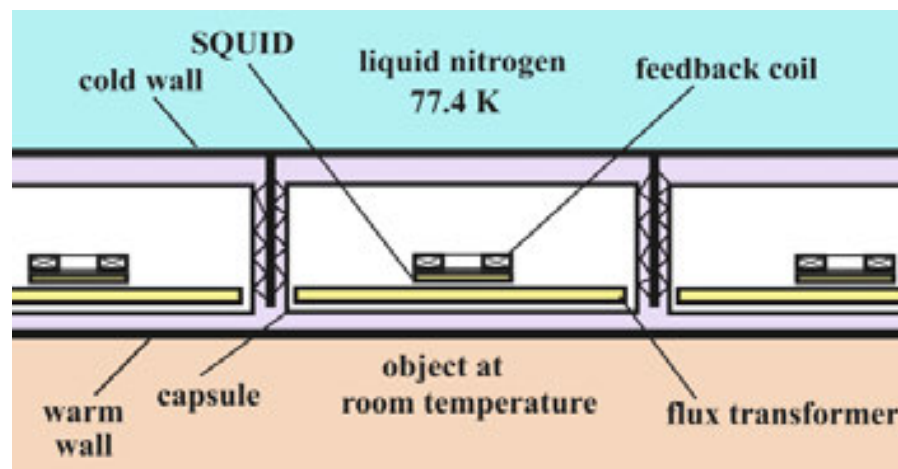**Figure 23.** Schematic view of an array of HTM-D20 magnetometers cooled sidewards in the vacuum space of a liquid nitrogen cryostat.

When constructing the cryostat holder or gantry for a multichannel high-T$_c$ MEG system, one should take into account that the density of liquid nitrogen (~0.8 kg/liter) is much higher than that of liquid helium (~0.128 kg/liter). A typical 50 liter cryostat for MEG would be ~33 kg

heavier if it would be filled with liquid nitrogen. This may require modifications of contemporary gantries for low-T$_c$ MEG systems.

Acknowledgements

Author details

M. I. Faley[1,4], O. M. Faley[2,4], U. Poppe[3], U. Klemradt[2,4] and R. E. Dunin-Borkowski[1,4]

*Address all correspondence to: m.faley@fz-juelich.de

1 Forschungszentrum Jülich GmbH, Jülich, Germany

2 RWTH Aachen University, Aachen, Germany

3 CEOS GmbH, Heidelberg, Germany

4 Jülich-Aachen Research Alliance in Future Information Technologies (JARA-FIT), Germany

References

[1] Wu, M. K. et al. Superconductivity at 93 K in a new mixed-phase Y-Ba-Cu-O compound system at ambient pressure. Phys. Rev. Lett. 1987;58 908–912.

[2] Li Y., Reeves J., Xiong X., Qiao Y., Xie Y., Hou P., Knoll A., Lenseth K., and Selvamanickam V., Fast growth process of long-length YBCO coated conductor with high critical current density. IEEE Trans. Appl. Supercond. 2005;15(2) 2771-2774.

[3] Faley M. I., Poppe U., Dunin-Borkowski R. E., Schiek M., Boers F., Chocholacs H., Dammers J., Eich E., Shah N. J., Ermakov A. B., Slobodchikov V. Yu., Maslennikov Yu. V., and Koshelets V. P. High-T$_c$ DC SQUIDs for magnetoencephalography, IEEE Trans. Appl. Supercond., 2013;23(3) 1600705(5).

[4] Faley M. I. Epitaxial oxide heterostructures for ultimate high-T$_c$ quantum interferometers. In Adir Luiz A. (ed.) Applications of High-T$_c$ Superconductivity. Rijeka: In-Tech; 2011 p.147-176. http://www.intechopen.com/books/show/title/applications-of-high-tc-superconductivity. (accessed 12 September 2014).

[5]   Commonwealth Scientific and Industrial Research Organisation. CSIRO: LANDTEM: helping to unearth A$6bn dollars in mineral deposits. http://www.csiro.au/Organisa-tion-Structure/Divisions/CMSE/Our-stories/Landtem.aspx. (accessed 12 September 2014).

[6]   Tanaka S., Fujita H., Hatsukade Y., Nagaishi T., Nishi K., Ota H., Otani T., and Suzu-ki S. High Tc SQUID Based Metallic Contaminant Detection System for Beverage or Ground Meat, IEEE Trans. Appl. Supercond. 2007;17(2) 756-759.

[7]   Huang K.-W., Chieh J.-J., Lin I.-T., Horng H.-E., Yang H.-C. and Hong C.-Y., Anti-CEA-functionalized superparamagnetic iron oxide nanoparticles for examining col-orectal tumors in vivo. Nanoscale Research Letters. 2013;8 413(8).

[8]   Szot K., Dittmann R., Speier W., and Waser R. Nanoscale resistive switching in $SrTiO_3$ thin films. Phys. Stat. Sol. 2007;1(2) R86–R88.

[9]   Cen C., Thiel S., Hammerl G., Schneider C. W., Andersen K. E., Hellberg C. S., Man-nhart J. and Levy J. Nanoscale control of an interfacial metal–insulator transition at room temperature. Nature Materials. 2008;7 298-302.

[10]   Sawa A. (2008). Resistive switching in transition metal oxides, Materials Today, Vol. 12, N.6, pp.28-36.

[11]   Szot K., Bihlmayer G., Speier W., Chapter 4-Nature of the resistive switching phe-nomena in TiO_2 and $SrTiO_3$: Origin of the Reversible Insulator–Metal Transition. Sol-id State Physics. 2014(65) 353-559.

[12]   Shkuratov S. I., Mesyatz V. G., Ivanov S. N. and Yumaghuzin Yu.M., Field emission electron spectroscopy of high temperature superconductors. Superconductivity: Physics, Chemistry, Technique. 1990;3(6) 1145-1221 (in Russian).

[13]   Hirano T., Ueda M., Matsui K.-i., Fujii T., Sakuta K., and Kobayashi T., Dielectric properties of $SrTiO_3$ epitaxial film and their application to measurement of work function of $YBa_2Cu_3O_y$ epitaxial film. Jpn. J. Appl. Phys. 1992;31 1345.

[14]   Li K., Wen Z., Wu D., Zhai H. and Li A., Bipolar resistive switching based on $SrTiO_3/YBa_2Cu_3O_7$ epi-layers, J. Phys. D: Appl. Phys. 2013(46) 035308.

[15]   Yang Q., Zhang H., Dai Q., Nie R. and Wang F. The abnormal temperature-depend-ent rectification effect in $BiFeO_3/YBa_2Cu_3O_x$ heterostructures. Journal of Physics: Con-ference Series. 2014;507 012052(5).

[16]   Poppe, U., Klein, N., Dähne, U., Soltner, H., Jia, C. L., Kabius, B., Urban. K., Lubig, A., Schmidt, K., Hensen, S., Orbach, S., Müller, G., & Piel, H. Low resistivity epitaxial $YBa_2Cu_3O_7$ thin films with improved microstructure and reduced microwave losses, J. Appl. Phys., 1992;71 5572-5578.

[17]   Faley M. I., and Poppe U. Sputtering sources for high-pressure sputtering with large targets   and   sputtering   method.   Patent   WO2012051980   (26.04.2012),

US20130199924A1 (08.08.2013), CN 103168338 A (19.06.2013). Priority date 22.10. 2010.

[18] Erni R., Rossell M. D., Kisielowski C., and Dahmen U. Atomic-Resolution Imaging with a Sub-50-pm Electron Probe, Phys. Rev. Lett. 2009;102 096101.

[19] Uhlemann S., Müller H., Hartel P., Zach J., and Haider Max. Thermal Magnetic Field Noise Limits Resolution in Transmission Electron Microscopy, Phys Rev. Lett. 2013;111 046101.

[20] Faley M. I. and Poppe U. Supraleitender Magnetfeldstabilisator, Patent pending DE102014003536. (2014).

[21] Buckel W. and Kleiner R. Supraleitung. (2013). ISBN 978-3-527-41139-9.

[22] The Conductus® Superconducting Wire Manufacturing Process: http://www.suptech.com/the_conductus_process_n.php. (accessed 12 September 2014).

[23] Oisjoen F., Schneiderman J. F., Figueras G. A., Chukharkin M. L., Kalabukhov A., Hedstrom A., Elam M., Winkler D. High-T$_c$ superconducting quantum interference device recordings of spontaneous brain activity: Towards high-Tc magnetoencephalography. Applied Physics Letters. 2012;100 132601.

[24] Peplow M. US bill would keep helium store afloat. Nature. 2013;497 168–9.

[25] Good J. Comment: Solving the liquid helium problem. Materials Today. 2014;17(1) 2-3.

[26] Faley M.I., Poppe U., Urban K., Paulson D.N., and Fagaly R.L. A new generation of the HTS multilayer DC-SQUID magnetometers and gradiometers. Journal of Physics: Conference Series. 2006;43 1199-1202.

[27] "Elekta Neuromag® System Hardware", Technical manual, Revision F (2005).

[28] Schneiderman J.F. Information content with low-vs. high-Tc SQUID arrays in MEG recordings: The case for high-Tc SQUID-based MEG. Journal of Neuroscience Methods. 2014;222 42– 46.

[29] Dammers J., Chocholacs H., Eich E., Boers F., Faley M., Dunin-Borkowski R. E. and Shah N. J. Source localization of brain activity using helium-free interferometer. Appl. Phys. Lett. 2014;104 213705.

[30] Faley M.I., Meertens D., Poppe U., Dunin-Borkowski R.E. Graphoepitaxial Josephson junctions and DC SQUIDs. 14th International Superconductive Electronics Conference (ISEC) 7-11 July 2013, IEEE Xplore Digital Library. 2013 1-3. doi: 10.1109/ISEC. 2013.6604264.

[31] Faley M. I. Reproduzierbarer Stufen-Josephson-Kontakt. Patent DE 102012006825 A1 (10.10.2013).

[32] Mitchell E. E. and Foley C. P. YBCO step-edge junctions with high I_cR_n. Supercond. Sci. Technol. 2010;23 065007.

[33] Clarke J., "SQUID Fundamentals", in: H. Weinstock (Ed.), SQUID Sensors: Fundamentals, Fabrication and Applications (NATO ASI Series E: Applied. Science. 329), Kluwer Academic, Dordrecht, 1996 p.1–62.

[34] Schmelz M., Stolz R., Zakosarenko V., Anders S., Fritzsch L., Roth H., Meyer H.-G. Highly sensitive miniature SQUID magnetometer fabricated with cross-type Josephson tunnel junctions. Physica C. 2012;478 77–80.

[35] Faley M. I., Poppe U., Urban K., Paulson D. N., Starr T., and Fagaly R. L. Low noise HTS dc-SQUID flip-chip magnetometers and gradiometers. IEEE Transactions on Appl. Supercond. 2001;11(1) 1383-1386.

[36] Matlashov A., Bakharev A., Zhuravlev Y., and Slobodchikov V. Biomagnetic multi-channel system consisting of several self-contained autonomous small-size units. In: Koch H. and Lübbig H. (ed.) Superconducting Devices and Their Applications. Berlin: Springer-Verlag; 1992;64 511-516.

[37] Fagaly R. L. Neuromagnetic instrumentation. In: Sato S. (ed.) Advances in Neurology. New York: Raven Press; 1990;54: Magnetoencephalography 11-32.

[38] Malmivuo J. Comparison of the Properties of EEG and MEG in Detecting the Electric Activity of the Brain. Brain Topography. 2012;25 1–19.